

# Exploring magnetic anisotropy and robustness of the $J_{\text{eff}} = 1/2$ state under substantial orthorhombic distortion in $\text{Sr}_2\text{IrO}_4$ thin films


S. Shrestha<sup>1,\*</sup>, Y. Choi<sup>2</sup>, M. Krautloher<sup>3</sup>, M. Zhu<sup>4</sup>, J. Hwang<sup>4</sup>, B. Keimer<sup>3</sup>, A. Seo<sup>1,†</sup> and J.-W. Kim<sup>2,‡</sup>

<sup>1</sup>*Department of Physics and Astronomy, University of Kentucky, Lexington, Kentucky 40506, USA*

<sup>2</sup>*Advanced Photon Source, Argonne National Laboratory, Argonne, Illinois 60439, USA*

<sup>3</sup>*Max-Planck-Institut für Festkörperforschung, D-70569 Stuttgart, Germany*

<sup>4</sup>*Department of Materials Science and Engineering, The Ohio State University, Columbus, Ohio 43210, USA*

 (Received 30 October 2023; revised 31 January 2024; accepted 21 February 2024; published 14 March 2024)

We present a comprehensive study revealing the intricate interplay of the magnetic anisotropy and orthorhombic distortion in thin films of  $\text{Sr}_2\text{IrO}_4$  through a  $\text{Ca}_3\text{Ru}_2\text{O}_7$  substrate. By inducing a pronounced orthorhombic distortion along the direction of oxygen octahedral edges, we effectively modulated the uniaxial magnetic anisotropy in the system. Remarkably divergent responses along the easy and hard magnetic axes were unveiled through x-ray magnetic circular dichroism (XMCD) measurements under magnetic fields. Specifically, the spin flop transition observed when the magnetic field aligns with the hard axis allows us to estimate the magnetic anisotropy energy, which is around  $14.2 \mu\text{eV}$ , close to that estimated from the single magnon peak measured via Raman spectroscopy. The observed anisotropy energy remains notably lower than the linear estimates derived from the strain-anisotropy energy relationship outlined in H.-H. Kim *et al.*, *Nat. Commun.* **13**, 6674 (2022). This underscores the enduring preservation of the isotropic character of the  $J_{\text{eff}} = 1/2$  states. This is also supported by the negligible XMCD intensity ratio at the  $L_2$  edge compared to that of the  $L_3$  edge. Furthermore, the branching ratio determined from x-ray absorption spectroscopy shows that the expectation value of the spin-orbit coupling is similar to that of bulk  $\text{Sr}_2\text{IrO}_4$  single crystals. Our findings indicate that even under a substantial anisotropic biaxial distortion,  $\text{Sr}_2\text{IrO}_4$  remains remarkably proximate to the  $J_{\text{eff}} = 1/2$  state. This study not only provides valuable information in understanding the interplay between magnetic anisotropy and strain but also the robustness of the  $J_{\text{eff}} = 1/2$  state under octahedral distortion within materials exhibiting emergent quantum phenomena.

DOI: [10.1103/PhysRevB.109.104415](https://doi.org/10.1103/PhysRevB.109.104415)

## I. INTRODUCTION

Iridates provide a fertile ground for exploring different properties due to the coexistence of strong spin-orbit interaction and electron correlation [1]. Particularly, iridium compounds featuring  $d^5$  ions within local  $\text{IrO}_6$  octahedral environments serve as a central focus in the pursuit of these interesting properties. Due to the crystal field effect, the five  $d$  electrons reside in sixfold degenerate  $t_{2g}$  orbitals, which are significantly split by strong spin-orbit interaction into a fully occupied lower  $J_{\text{eff}} = 3/2$  quartet and a half-filled upper  $J_{\text{eff}} = 1/2$  doublet. Even the modest electron correlation produces a spin-orbit Mott insulator with a  $J_{\text{eff}} = 1/2$  pseudospin ground state [2]. This exotic state provides a platform for investigating quantum spin liquid in a honeycomb lattice [3–5] and a possibility of superconductivity in single layered iridates with a square lattice such as  $\text{Sr}_2\text{IrO}_4$  and  $\text{Ba}_2\text{IrO}_4$  [6–8].

The ideal  $J_{\text{eff}} = 1/2$  wave function is based on the local cubic symmetry having perfect  $\text{IrO}_6$  octahedra with multi-orbital characteristics [9]. In contrast to the  $S = 1/2$  spin, the  $J_{\text{eff}} = 1/2$  state has equal contributions from  $d_{xy}$ ,  $d_{yz}$ ,

and  $d_{zx}$  orbitals and is expressed as  $|J_{\text{eff}} = \frac{1}{2}, m_{J_{\text{eff}}} = \pm \frac{1}{2}\rangle = \frac{1}{\sqrt{3}}(|d_{yz}, \pm\sigma\rangle \mp |d_{xy}, \mp\sigma\rangle + i|d_{zx}, \pm\sigma\rangle)$ , where  $\sigma$  is the spin and  $d_{xy}$ ,  $d_{yz}$ , and  $d_{zx}$  are the  $t_{2g}$  orbitals of the  $5d$  electrons [10]. By lowering the crystal symmetry, e.g., increasing structural distortion, the  $J_{\text{eff}} = 1/2$  pseudospin picture may become invalid since the degeneracy of the  $t_{2g}$  orbitals can be removed, as shown in Fig. 1.

The distortion of oxygen octahedral cages is often found in iridate systems which exhibit intriguing quantum phenomena [11–15]. This distortion inevitably impacts the ideal  $J_{\text{eff}} = 1/2$  state, which is expected to exhibit equal contributions from the  $d_{xy}$ ,  $d_{yz}$ , and  $d_{zx}$  orbitals. This gives rise to a fundamental question: To what extent does the distortion of these oxygen octahedra influence the behavior of these iridate systems?

Previous orthorhombic strain measurements were limited to a small strain range, using bulk single crystals and piezoelectric strain cells [16–18]. Even within this limited strain range, typically less than  $\sim 0.1\%$ , the metamagnetic transition field still underwent significant alterations [18], and the single magnon gap exhibited gradual increase [16]. This susceptibility emphasized the sensitivity of the magnetic anisotropy in the  $J_{\text{eff}} = 1/2$  state to strain.

In contrast, our recent study explored the magnetic configuration and the transition temperature of  $\text{Sr}_2\text{IrO}_4$  thin films subjected to substantial anisotropic strain [19]. This was

\*Corresponding author: [sshrestha2079@gmail.com](mailto:sshrestha2079@gmail.com)

†Corresponding author: [a.seo@uky.edu](mailto:a.seo@uky.edu)

‡Corresponding author: [jwkim@anl.gov](mailto:jwkim@anl.gov)

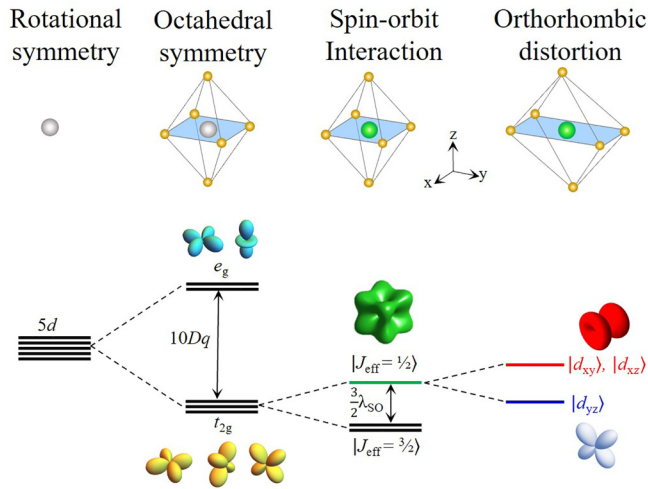


FIG. 1. Schematic diagram of 5d orbitals affected by crystal field, spin-orbit interactions, and anisotropic strain. Large anisotropic strain can remove the degeneracy of  $t_{2g}$  orbitals.

achieved through  $\text{Ca}_3\text{Ru}_2\text{O}_7$  (001) single crystals as a substrate, which encompassed a compressive strain of  $-2.21(7)\%$  along the  $[1\ 0\ 0]$  direction and a tensile strain of  $+0.93(7)\%$  along the  $[0\ 1\ 0]$  direction [Fig. 2(a)], far surpassing the achievable strain levels of conventional piezoelectric strain devices typically employed for single crystals [16–18]. Therefore, it is of particular interest to investigate the impact of this substantial orthorhombic distortion on the isotropic nature of the  $J_{\text{eff}} = 1/2$  state and its magnetic anisotropy in this system, especially in contrast to the minimal strains typically induced by conventional devices.

Despite this significant anisotropic strain, the magnetic transition temperature closely aligns with that of bulk single crystals, suggesting the dominant magnetic interactions are unchanged in the  $\text{Sr}_2\text{IrO}_4/\text{Ca}_3\text{Ru}_2\text{O}_7$  system. However, the orthorhombic structural arrangement lifts the magnetic structure degeneracy of the  $\text{Sr}_2\text{IrO}_4$  single crystal (AFM-1); one with the magnetic moment direction along  $[1\ 0\ 0]$  possesses  $(1\ 0\ 4n)$  and  $(0\ 1\ 4n + 2)$  allowed magnetic reflections and the other with the magnetic moment direction along  $[0\ 1\ 0]$  possesses  $(1\ 0\ 4n + 2)$  and  $(0\ 1\ 4n)$  allowed magnetic reflections. Consequently, the longer axis—the  $[0\ 1\ 0]$  direction—emerges as the preferred magnetic axis, and the magnetic order’s correlation length along the  $c$  axis matches the film thickness [17–19]. This displays clearly that the orthorhombic distortion eliminates the degeneracy associated with interlayer interactions and magnetic stacking along the  $c$  axis. For small orthorhombic distortion, the magnetic stacking order is still AFM-1. However, for large anisotropic strained  $\text{Sr}_2\text{IrO}_4$  thin film, we previously demonstrated that the magnetic stacking order is different from the bulk single crystal. Notably, the substantial orthorhombic distortion makes the nearest Ir atom in the next layer to be antiferromagnetically aligned by the interlayer exchange interaction (AFM-2), having been formally ferromagnetically ordered by the pseudodipolar interaction for small uniaxial strain (AFM-1) [17,19]. Establishing a magnetic single domain enables the comprehensive exploration of  $\text{Ir}^{4+}$  moments’ response to external magnetic fields.

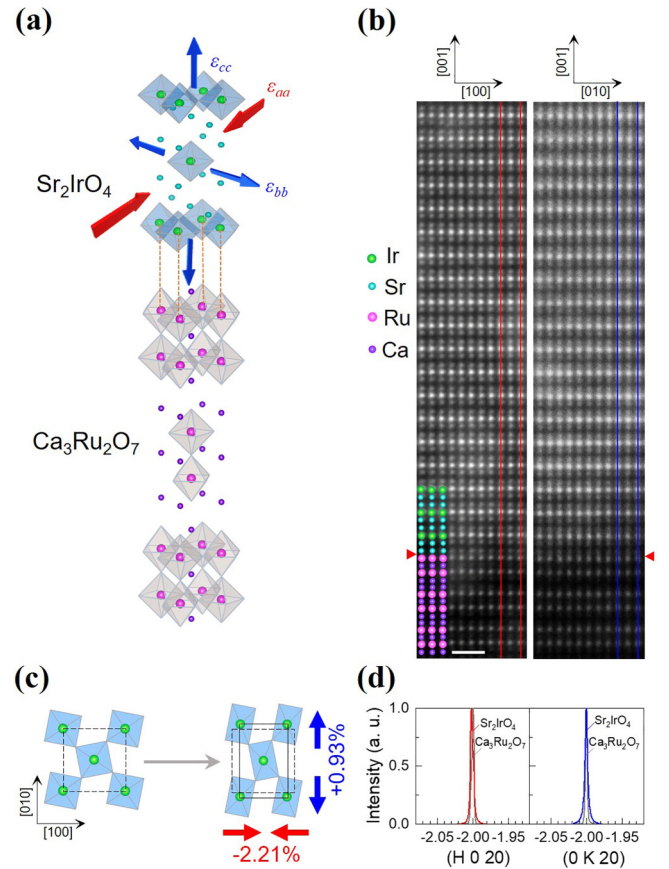


FIG. 2. (a) Schematic diagram of  $\text{Sr}_2\text{IrO}_4/\text{Ca}_3\text{Ru}_2\text{O}_7$  heterostructure with red arrow and blue arrow representing the compressive strain and tensile strain, respectively, along the specific directions. (b) The high-resolution Z-contrast scanning transmission electron microscopy images of a  $\text{Sr}_2\text{IrO}_4/\text{Ca}_3\text{Ru}_2\text{O}_7$  heterostructure for both  $[1\ 0\ 0]$  and  $[0\ 1\ 0]$  lattice directions. The two red and blue lines show that  $\text{Sr}_2\text{IrO}_4$  thin films are perfectly strained along both  $[1\ 0\ 0]$  and  $[0\ 1\ 0]$  lattice directions, respectively, over the whole thickness. The red triangles mark the atomically sharp interface between  $\text{Sr}_2\text{IrO}_4$  and  $\text{Ca}_3\text{Ru}_2\text{O}_7$ . The scale bar is 1 nm. (c) The possible distortion of the  $ab$  plane of the octahedra due to the  $-2.21\%$  compressive strain along  $a$  axis and  $+0.93\%$  tensile strain along  $b$  axis at 6 K. (d)  $H$  and  $K$  scans of  $\text{Sr}_2\text{IrO}_4$  thin film and  $\text{Ca}_3\text{Ru}_2\text{O}_7$  substrate showing perfect alignment of  $a$ - and  $b$ -lattice constant of  $\text{Sr}_2\text{IrO}_4$  thin film with respect to the  $\text{Ca}_3\text{Ru}_2\text{O}_7$  substrate. The  $H$  and  $K$  scans were conducted for the  $\text{Ca}_3\text{Ru}_2\text{O}_7$  substrate around its  $(2\ 0\ 16)$  and  $(0\ 2\ 16)$  reflections, and for the  $\text{Sr}_2\text{IrO}_4$  thin films around its  $(2\ 0\ 20)$  and  $(0\ 2\ 20)$  reflections, respectively. The  $H$  and  $K$  scans were measured with the wavelength of  $1.1055\ \text{\AA}$ , at the 6-ID-B beamline of the Advanced Photon Source (APS).

In this work, we performed x-ray magnetic circular dichroism (XMCD) measurements at the Ir  $L_2$  and  $L_3$  absorption edges to examine the response of the weak ferromagnetic alignment with respect to the direction and strength of the field, aiming to estimate the magnetic anisotropy of this highly strained system. The estimated magnetic anisotropy is close to that obtained using single magnon peak energy measured via Raman spectroscopy. Moreover, we examined the white line branching ratio derived from x-ray absorption spectroscopy

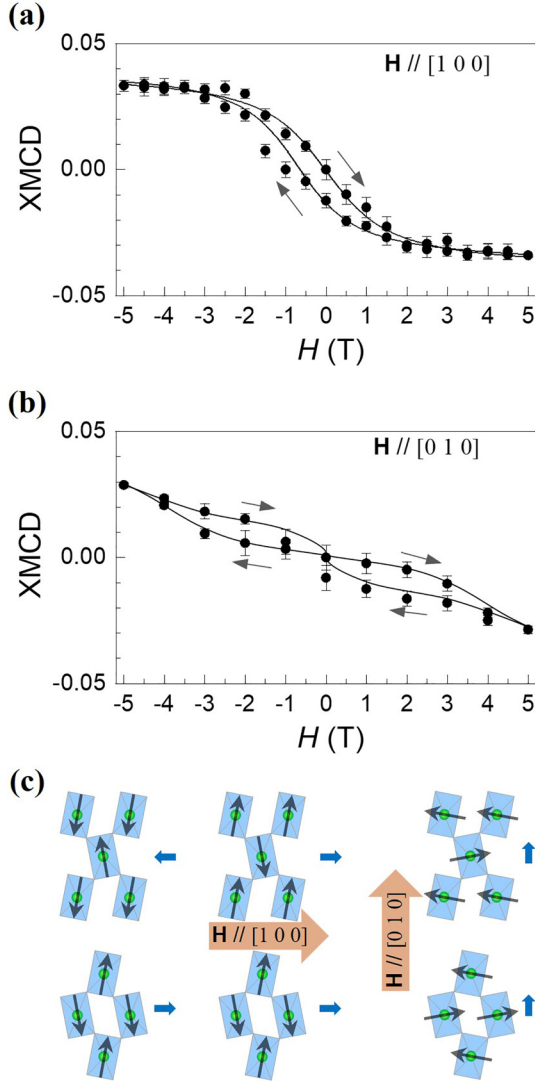


FIG. 3. The hysteresis loop of XMCD intensities measured at Ir  $L_3$  edge by applying external magnetic fields along (a)  $[1 0 0]$  lattice direction and (b)  $[0 1 0]$  lattice direction. The values of XMCD intensities were obtained by using Lorentzian curve fits. The black solid lines are the eye guide for the hysteresis curve. The gray arrows represent the direction of the measurement of the XMCD for different magnetic fields. (c) The schematic diagrams represent the initial  $J_{\text{eff}} = 1/2$  pseudospin configuration and the configuration when the saturated magnetic field is applied along  $[1 0 0]$  and  $[0 1 0]$ , respectively.

(XAS) to explore the alterations in spin-orbit coupling induced by uniaxial distortion.

## II. EXPERIMENT

To achieve a substantially large anisotropic strain, we deposited  $\text{Sr}_2\text{IrO}_4$  thin films onto a  $\text{Ca}_3\text{Ru}_2\text{O}_7$  single crystal, which has lattice constants of  $a = 5.367 \text{ \AA}$ ,  $b = 5.536 \text{ \AA}$ , and  $c = 19.521 \text{ \AA}$  at 8 K [20]. The 24-nm-thick  $\text{Sr}_2\text{IrO}_4$  epitaxial thin films were deposited using pulsed laser deposition under the conditions of  $700^\circ\text{C}$  substrate temperature,  $1.2 \text{ J/cm}^2$  laser fluence, and 10 mTorr oxygen partial pressure. High-resolution Z-contrast scanning transmission electron

microscopy (STEM) images [(Fig. 2(b)), shows that  $\text{Sr}_2\text{IrO}_4$  thin film is strained along both  $a$ - and  $b$ -lattice constants and this is confirmed by the x-ray diffraction as shown in Fig. 2(d). Consequently, the lattice constants at 6 K were determined as  $a = 5.364(4) \text{ \AA}$ ,  $b = 5.536(4) \text{ \AA}$ , and  $c = 25.92(2) \text{ \AA}$ , resulting in compressive strain of  $\varepsilon_{aa} = -2.21(7)\%$  along the  $a$  direction, tensile strain of  $\varepsilon_{bb} = +0.93(7)\%$  along the  $b$  direction, and tensile strain of  $\varepsilon_{cc} = +0.47(8)\%$  along the  $c$  direction. These lattice constants correspond to the large orthorhombic distortion [ $\alpha \equiv (b - a) / (b + a)$ ] of  $+1.58\%$ .

Figure 2(c) visually represents the potential alterations in the  $\text{IrO}_6$  octahedral structure, which can be attributed to the presence of anisotropic biaxial strain. When subject to isotropic biaxial strain—meaning equal amounts of tensile or compressive strain applied along both in-plane directions—the rotation of the  $\text{IrO}_6$  octahedra adjusts accordingly. For instance, tensile strain reduces the rotation angle, whereas compressive strain increases it, as documented in previous studies [21,22]. However, the influence of anisotropic biaxial strain on octahedral rotation might not exhibit such straightforward behavior. The adjustment induced by this strain pattern could potentially involve transforming the  $ab$ -plane configuration of the  $\text{IrO}_6$  octahedra from a square shape into a rectangular one.

XMCD and XAS were measured at the Ir absorption edges of the  $\text{Sr}_2\text{IrO}_4$  thin film under cryogenic conditions (10 K) using a superconducting magnet at the beamline 4-ID-D at APS. These XAS measurements were performed in fluorescence mode, employing an energy-dispersive detector. The XMCD spectrum is obtained as the difference between the two XAS spectra with right and left circular polarization. Throughout the measurements, a magnetic field up to 5 T was applied along the in-plane directions  $[1 0 0]$  and  $[0 1 0]$  of the sample. The x-ray beam was also maintained along the same direction with an incident angle of approximately  $5^\circ$  relative to the surface. XAS spectra at Ir  $L_2$  and  $L_3$  absorption edges are normalized to the edge jump, respectively, and XMCD is also normalized accordingly.

Raman spectra for the  $\text{Sr}_2\text{IrO}_4$  thin film were acquired using a confocal micro-Raman spectrometer (JobinYvon LabRam HR800) with a focused beam spot size of approximately  $5 \mu\text{m}$ . The excitation source utilized was a HeNe laser with a wavelength of 632.8 nm, and the spectrometer featured a 600-grooves/mm grating, resulting in an energy resolution of approximately  $5 \text{ cm}^{-1}$ .

## III. RESULTS AND DISCUSSION

Due to the anisotropic strain,  $\text{Sr}_2\text{IrO}_4/\text{Ca}_3\text{Ru}_2\text{O}_7$  heterostructure show AFM-2 magnetic structure having the direction of antiferromagnetic ordered moments along the  $[0 1 0]$  direction with the weak canted ferromagnetic moment along the  $[1 0 0]$  direction [19]. Initially, the sample was mounted with the external magnetic field oriented along the  $[1 0 0]$  direction, which aligns with the direction parallel to the canted ferromagnetic component. The magnetic field sequence employed for the XMCD measurements is 0 to 5 T, 5 to 0 T, 0 to  $-5$  T, and  $-5$  to 0 T. The field-dependent XMCD values display a characteristic hysteresis loop, as shown in Fig. 3. At the  $L_3$  edge, the XMCD signal progressively increases with



the magnetic field. Around 2.5 T, the XMCD signal saturates and at 5 T, the dichroic signal reaches 0.03% of the  $L_3$  edge absorption jump. This is comparable to the bulk XMCD measurements having AFM-1 magnetic structure, suggesting that the canted ferromagnetic moments remain similar to those in the bulk configuration, even within the presence of substantial uniaxial distortion [23]. Note that the net pseudospin magnetic moment corresponding to the 0.03% of XMCD is about  $0.045 \mu_B/\text{Ir}$  [23]. Since canted moments are rigidly locked with  $\text{IrO}_6$  octahedra through the Dzyaloshinskii-Moriya interaction, the comparable canted ferromagnetic moments imply that this rotation perseveres despite the significant distortion [24,25]. In  $\text{Sr}_2\text{IrO}_4$  thin films grown by PLD, the oxygen octahedral rotation does not exhibit coherence along the crystallographic  $c$  axis [26]. Consequently, unlike in bulk crystals, the canted moments lack coherent alignment along the  $c$  axis, while main moments are well ordered in the absence of a magnetic field. When a sufficiently strong external magnetic field is applied, the canted ferromagnetic moments align uniformly with the field direction [Fig. 3(c)], leading to a disruption in the alignment of the main magnetic moments along the  $c$  axis. This marked distinction from the bulk material explains the absence of a metamagnetic transition observed in the  $\text{Sr}_2\text{IrO}_4$  thin films [Fig. 3(a)]. Within the hysteresis loop, the coercivity field measures approximately 0.5 T, and the remanence is found to be less than one-third of the saturated moment. This observation implies that when the magnetic field is removed, the magnetic moment predominantly reverts to its original state, characterized by the antiferromagnetic alignment [27].

Conversely, when the magnetic field is oriented along the  $[0\ 1\ 0]$  direction, which is orthogonal to the canted moment direction, the XMCD signal shows only a marginal increase until  $\sim 2$  T [Fig. 3(b)]. However, beyond this threshold, the signal exhibits a rapid upsurge. This increase in signal can be explained by the canted ferromagnetic moment rotating towards the hard axis direction when subjected to the applied field as shown in Fig. 3(c). Initially, it is oriented along the easy axis, but as the magnetic field strength surpasses 2 T, it overcomes the uniaxial magnetic anisotropy caused by the orthorhombic lattice distortion. The uniaxial magnetic anisotropy measures approximately  $14.2 \mu\text{eV}$  which corresponds to the Zeeman energy estimated from the spin flop transition occurring at approximately 3.5 T. The Zeeman energy value closely matches the calculated magnetic anisotropy of  $18.9 \mu\text{eV}$ , which is determined from the energy of the single magnon peak at  $44 \text{ cm}^{-1}$  ( $5.5 \text{ meV}$ ), as depicted in Fig. 4 [16]. Similar spin-flop transition was observed in the AFM-1 magnetic structure of 0.054% uniaxially strained  $\text{Sr}_2\text{IrO}_4$  bulk resulting in the increased spin-flop transition field of 0.23 T, more than 15 times smaller than that of  $\text{Sr}_2\text{IrO}_4/\text{Ca}_3\text{Ru}_2\text{O}_7$  heterostructure [18].

In the previous investigations, uniaxial magnetic anisotropy was assessed by introducing mechanical strain to deform the bulk crystal into an orthorhombic structure. Please note that the detwinned AFM-1 magnetic structure was stabilized for small uniaxial strain and the uniaxial magnetic anisotropy was estimated to be about 31 neV by using a two slab-cell model. Using this model, the uniaxial anisotropy is estimated to take the form  $K_u = \lambda \varepsilon M^2$ , where  $\lambda$  is the magnetic coupling coefficient,  $\varepsilon$  is the uniaxial strain value, and  $M$  is the local moment. Using a similar

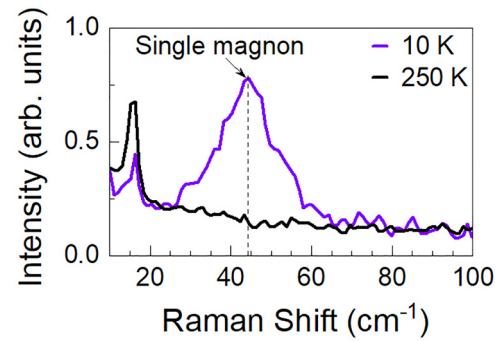


FIG. 4. Raman spectra of a  $\text{Sr}_2\text{IrO}_4/\text{Ca}_3\text{Ru}_2\text{O}_7$  heterostructure in the low-energy region revealing a  $B_{2g}$  single magnon peak at  $44 \text{ cm}^{-1}$  at 10 K.

relationship between strain and magnetic uniaxial anisotropy, the linearly estimated total anisotropy energy resulting from substrate-induced strain in both the  $a$  and  $b$  directions ( $-2.2\%$  and  $+0.94\%$ , respectively) is approximately  $2.4 \mu\text{eV}$  [18]. This value is significantly smaller—eight times less—than the magnetic anisotropy of  $18.9 \mu\text{eV}$ . The coefficient of the strain induced magnetic anisotropy was obtained at 210 K in the previous study while the XMCD measurement was performed at 10 K and even slight uncertainties in the strain measurements can yield substantial disparities in estimations within the context of large strain.

Another study considered the alteration in single magnon energy with uniaxial strain, as determined through Raman spectroscopy [16]. It showed that the pseudospin lattice coupling explains the shift in the single magnon peak with respect to strain. Furthermore, the single magnon excitation energy, that corresponds to the magnetic anisotropy, increases linearly with both compressive and tensile uniaxial strain [16] and it is explained by the equation  $\Delta = \Delta_0 \sqrt{1 + \frac{|\varepsilon|}{\varepsilon_0}}$ , where  $\Delta$  is the single magnon energy at the uniaxial strain of  $\varepsilon$  and  $\Delta_0 = 2.23 \text{ meV}$  is the single magnon energy at the intrinsic uniaxial strain of  $\varepsilon_0 = 1.18 \times 10^{-3}$ . Using this equation, the estimated single magnon energy at the 2.2% strain level surges to  $9.88 \text{ meV}$ , resulting in the magnetic anisotropy of  $61 \mu\text{eV}$  obtained from the relation  $\Delta = 8S\sqrt{J\Gamma}$ , where  $S$  is the spin quantum number,  $J$  is the in-plane exchange interaction, and  $\Gamma$  is the magnetic anisotropy [28]. Furthermore, the magnetic field corresponding to this single magnon energy value is equivalent to a Zeeman energy at  $\sim 30$  T, substantially higher than the estimated value of this work [29].

It is important to acknowledge that, in the previous two studies, the coefficients were estimated based on measurements with relatively small strain. Consequently, linear extrapolation may not be valid to estimate the anisotropy energy in the significantly higher strain state. Our observation clearly shows that the magnetic anisotropy does not strongly increase with substantial anisotropic biaxial strain ( $-2.2\%$  and  $+0.94\%$  along the  $[1\ 0\ 0]$  and  $[0\ 1\ 0]$  directions, respectively) suggesting that the spin-orbit entangled state undergoes no dramatic alteration, even in the presence of pronounced octahedral distortion.

The strength of spin-orbit coupling, as determined through the XAS white line branching ratio (BR), provides further

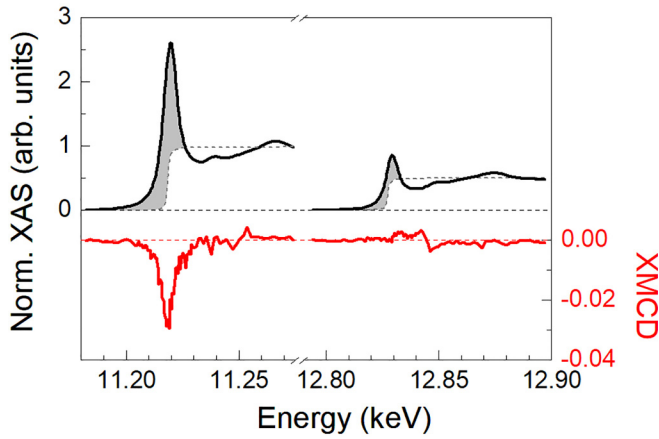


FIG. 5. XMCD and XAS measured at Ir  $L_3$  and  $L_2$  absorption edges with the external magnetic field applied along the  $b$  axis at 10 K. The XAS spectra is obtained as the average of the XAS spectra with right and left circular polarizations. The gray shaded area represents the experimentally determined integrated intensity of the white line. The gray dashed line represents the arctangent function, centered at the absorption edge. The peak in between 12.84 and 12.85 keV of XMCD is an artifact. This artifact at the Ir  $L_2$  edge is due to some imperfection in the beamline optics components, for instance single crystal diamond used as phase retarding optics to generate circular polarization. Similar features at the same energy range have been observed in Refs. [32–34] measured at the same beamline.

support for our findings. This branching ratio is computed using the formula  $BR = I_{L_3}/I_{L_2}$ , where  $I_{L_2}$  and  $I_{L_3}$  represent the integrated intensities associated with the  $2p \rightarrow 5d$  electronic transitions at the  $L_2$  and  $L_3$  absorption edges, respectively. To accurately extract the white-line integrated intensities from our data, we employ the continuum edge-step model using an arctangent function, denoted by the gray dashed line in Fig. 5. The arctangent function, centered at the absorption edges, is defined to have heights 0.5 and 1 for the  $L_2$  and  $L_3$  absorption edges, respectively. This arctangent function effectively removes the background, leaving us with the numerically integrated intensity solely contributed by the white-line feature. This method offers the advantage of not relying on the specific choice of line forms or fitting functions [30]. The calculated branching ratio of  $4.6 \pm 0.2$  aligns with values typically observed in  $\text{Sr}_2\text{IrO}_4$  single crystals [23,31]. The branching ratio then allows us to compute the ground state expectation value of the spin-orbit coupling operator  $\langle \mathbf{L} \cdot \mathbf{S} \rangle$  of  $5d$  states using  $\langle \mathbf{L} \cdot \mathbf{S} \rangle = \langle n_h \rangle (BR - 2)/(BR + 1)$ , where  $\langle n_h \rangle$  refers to the average number of holes in  $5d$  orbitals. The calculated  $\langle \mathbf{L} \cdot \mathbf{S} \rangle$  value stands at  $2.3\hbar^2$ , which is an indicative of robust spin-orbit coupling effects [23]. This value closely aligns with the  $J_{\text{eff}} = 1/2$  picture for the  $\text{Ir}^{4+}$  underscoring the well-preserved spin-orbit entangled state within  $\text{Sr}_2\text{IrO}_4$  thin film even in the presence of substantial anisotropic strain.

Additional corroborating evidence is found in the relatively weak XMCD intensity observed at the  $L_2$  edge. Generally, x-ray resonant magnetic scattering (XRMS) intensity at the

Ir- $L_2$  and  $L_3$  edges provide an evidence for the presence of the  $J_{\text{eff}} = 1/2$  state [10] given that the  $J_{\text{eff}} = 3/2$  band is fully occupied and  $J_{\text{eff}} = 1/2$  band is half filled [10]. Note that any deviation from the ideal  $J_{\text{eff}} = 1/2$  state results in nonzero intensity at the  $L_2$  edge, while a complete breakdown into  $d$  orbitals equalizes the transition probability for XRMS and XMCD at both  $L_2$  and  $L_3$  edges. Figure 5 shows that the apparent XMCD intensity at the  $L_3$  edge is observed while XMCD intensity at the  $L_2$  edge is notably weak, measuring over ten times smaller than that at the  $L_3$  edge. The weak XMCD in the  $L_2$  edge is consistent with the  $\text{Sr}_2\text{IrO}_4$  single crystal [23] considering that the  $\text{Ir}^{4+}$   $5d$  state is dominantly the  $J = 5/2$  state allowing the transition at the  $L_3$  edge while inhibiting any transition at the  $L_2$  edge. Thus, negligible XMCD intensity at the  $L_2$  edge compared to that of the  $L_3$  edge clearly supports the well-preserved spin-orbit entangled state.

#### IV. CONCLUSION

We investigated the magnetic characteristics of  $\text{Sr}_2\text{IrO}_4$  thin films subjected to substantial anisotropic strain via XMCD measurements. The anisotropic strain leads to the orthorhombic distortion to the  $\text{IrO}_6$  octahedra, inducing the observed in-plane magnetic anisotropy. The film exhibits spin-flop transitions when magnetic fields are applied perpendicular to the canted moment direction. The magnetic anisotropy energy, estimated at  $14.2 \mu\text{eV}$  from the Zeeman energy of the spin-flop transition at approximately 3.5 T, is significantly lower than the extrapolated value derived from the strain-magnetic anisotropy relationship established through Raman spectroscopy. This deviation suggests that the linear relation between the strain and magnetic anisotropy is not applicable at higher strain states. Even in the face of pronounced octahedral distortion imposed by the substrate, the spin-orbit entangled state remains preserved. The XAS and XMCD branching ratio data support the stability of the spin-orbit entangled state, with their characteristics reminiscent of the  $\text{Sr}_2\text{IrO}_4$  counterparts. Collectively, these findings present the remarkable resilience of the  $J_{\text{eff}} = 1/2$  states under significant octahedral distortion within materials that manifest emergent quantum phenomena.

#### ACKNOWLEDGMENTS

We acknowledge the support of National Science Foundation Grants No. DMR-2104296 and No. DMR-1847964 for sample synthesis and characterization. This research used resources of the Advanced Photon Source, a U.S. Department of Energy (DOE) Office of Science user facility at Argonne National Laboratory and is based on research supported by the U.S. DOE Office of Science-Basic Energy Sciences, under Contract No. DE-AC02-06CH11357. Electron microscopy was performed at the Center for Electron Microscopy and Analysis at the Ohio State University. B.K. acknowledges financial support from the Deutsche Forschungsgemeinschaft (DFG, German Research Foundation) through Project No. 107745057-TRR 80.

- [1] T. Takayama, J. Chaloupka, A. Smerald, G. Khaliullin, and H. Takagi, *J. Phys. Soc. Jpn.* **90**, 062001 (2021).
- [2] B. J. Kim, H. Jin, S. J. Moon, J. Y. Kim, B. G. Park, C. S. Leem, J. Yu, T. W. Noh, C. Kim, S. J. Oh *et al.*, *Phys. Rev. Lett.* **101**, 076402 (2008).
- [3] J. Chaloupka, G. Jackeli, and G. Khaliullin, *Phys. Rev. Lett.* **105**, 027204 (2010).
- [4] S. Hwan Chun, J.-W. Kim, J. Kim, H. Zheng, C. C. Stoumpos, C. D. Malliakas, J. F. Mitchell, K. Mehlawat, Y. Singh, Y. Choi *et al.*, *Nat. Phys.* **11**, 462 (2015).
- [5] G. Jackeli and G. Khaliullin, *Phys. Rev. Lett.* **102**, 017205 (2009).
- [6] Y. K. Kim, N. H. Sung, J. D. Denlinger, and B. J. Kim, *Nat. Phys.* **12**, 37 (2016).
- [7] J. Kim, D. Casa, M. H. Upton, T. Gog, Y.-J. Kim, J. F. Mitchell, M. van Veenendaal, M. Daghofer, J. van den Brink, G. Khaliullin *et al.*, *Phys. Rev. Lett.* **108**, 177003 (2012).
- [8] Y. K. Kim, O. Krupin, J. D. Denlinger, A. Bostwick, E. Rotenberg, Q. Zhao, J. F. Mitchell, J. W. Allen, and B. J. Kim, *Science* **345**, 187 (2014).
- [9] A. Abragam and B. Bleaney, *Electron Paramagnetic Resonance of Transition Ions* (Clarendon, Oxford, 1970).
- [10] B. J. Kim, H. Ohsumi, T. Komesu, S. Sakai, T. Morita, H. Takagi, and T. Arima, *Science* **323**, 1329 (2009).
- [11] M. K. Crawford, M. A. Subramanian, R. L. Harlow, J. A. Fernandez-Baca, Z. R. Wang, and D. C. Johnston, *Phys. Rev. B* **49**, 9198 (1994).
- [12] T. Hogan, L. Bjaalie, L. Zhao, C. Belvin, X. Wang, C. G. Van de Walle, D. Hsieh, and S. D. Wilson, *Phys. Rev. B* **93**, 134110 (2016).
- [13] J. P. Clancy, H. Gretarsson, J. A. Sears, Y. Singh, S. Desgreniers, K. Mehlawat, S. Layek, G. K. Rozenberg, Y. Ding, M. H. Upton *et al.*, *npj Quantum Mater.* **3**, 35 (2018).
- [14] A. A. Aczel, J. P. Clancy, Q. Chen, H. D. Zhou, D. Reig-i-Plessis, G. J. MacDougall, J. P. C. Ruff, M. H. Upton, Z. Islam, T. J. Williams *et al.*, *Phys. Rev. B* **99**, 134417 (2019).
- [15] T. Takayama, A. N. Yaresko, A. S. Gibbs, K. Ishii, D. Kukusta, and H. Takagi, *Phys. Rev. Mater.* **4**, 075002 (2020).
- [16] H.-H. Kim, K. Ueda, S. Nakata, P. Wochner, A. Mackenzie, C. Hicks, G. Khaliullin, H. Liu, B. Keimer, and M. Minola, *Nat. Commun.* **13**, 6674 (2022).
- [17] J.-W. Kim, S. H. Chun, Y. Choi, B. J. Kim, M. H. Upton, and P. J. Ryan, *Phys. Rev. B* **102**, 054420 (2020).
- [18] H. Zhang, L. Hao, J. Yang, J. Mutch, Z. Liu, Q. Huang, K. Noordhoek, A. F. May, J.-H. Chu, J.-W. Kim *et al.*, *Adv. Mater.* **32**, 2002451 (2020).
- [19] S. Shrestha, M. Krautloher, M. Zhu, J. Kim, J. Hwang, J. Kim, J. W. Kim, B. Keimer, and A. Seo, *Phys. Rev. B* **105**, L100404 (2022).
- [20] Y. Yoshida, S.-I. Ikeda, H. Matsuhata, N. Shirakawa, C. H. Lee, and S. Katano, *Phys. Rev. B* **72**, 054412 (2005).
- [21] J. Nichols, J. Terzic, E. G. Bittle, O. B. Korneta, L. E. De Long, J. W. Brill, G. Cao, and S. S. A. Seo, *Appl. Phys. Lett.* **102**, 141908 (2013).
- [22] E. Paris, Y. Tseng, E. M. Pärshcke, W. Zhang, M. H. Upton, A. Efimenko, K. Rolfs, D. E. McNally, L. Maurel, M. Naamneh *et al.*, *Proc. Natl. Acad. Sci. USA* **117**, 24764 (2020).
- [23] D. Haskel, G. Fabbris, M. Zhernenkov, P. P. Kong, C. Q. Jin, G. Cao, and M. van Veenendaal, *Phys. Rev. Lett.* **109**, 027204 (2012).
- [24] S. Boseggia, H. C. Walker, J. Vale, R. Springell, Z. Feng, R. S. Perry, M. Moretti Sala, H. M. Rønnow, S. P. Collins, and D. F. McMorrow, *J. Phys.: Condens. Matter* **25**, 422202 (2013).
- [25] D. H. Torchinsky, H. Chu, L. Zhao, N. B. Perkins, Y. Sizyuk, T. Qi, G. Cao, and D. Hsieh, *Phys. Rev. Lett.* **114**, 096404 (2015).
- [26] S. Geprägs, B. E. Skovdal, M. Scheufele, M. Opel, D. Wermeille, P. Thompson, A. Bombardi, V. Simonet, S. Grenier, P. Lejay *et al.*, *Phys. Rev. B* **102**, 214402 (2020).
- [27] C. Lu and J.-M. Liu, *Adv. Mater.* **32**, 1904508 (2020).
- [28] H. Liu and G. Khaliullin, *Phys. Rev. Lett.* **122**, 057203 (2019).
- [29] Y. Gim, A. Sethi, Q. Zhao, J. F. Mitchell, G. Cao, and S. L. Cooper, *Phys. Rev. B* **93**, 024405 (2016).
- [30] J. P. Clancy, N. Chen, C. Y. Kim, W. F. Chen, K. W. Plumb, B. C. Jeon, T. W. Noh, and Y.-J. Kim, *Phys. Rev. B* **86**, 195131 (2012).
- [31] M. A. Laguna-Marco, P. Kayser, J. A. Alonso, M. J. Martínez-Lope, M. van Veenendaal, Y. Choi, and D. Haskel, *Phys. Rev. B* **91**, 214433 (2015).
- [32] E. Skoropata, J. Nichols, J. M. Ok, R. V. Chopdekar, E. S. Choi, A. Rastogi, C. Sohn, X. Gao, S. Yoon, T. Farmer *et al.*, *Sci. Adv.* **6**, eaaz3902 (2020).
- [33] X. Liu, M. Kotiuga, H.-S. Kim, A. T. N'Diaye, Y. Choi, Q. Zhang, Y. Cao, M. Kareev, F. Wen, and B. Pal, *Proc. Natl. Acad. Sci. USA* **116**, 19863 (2019).
- [34] J. Nichols, X. Gao, S. Lee, T. L. Meyer, J. W. Freeland, V. Lauter, D. Yi, J. Liu, D. Haskel, J. R. Petrie *et al.*, *Nat. Commun.* **7**, 12721 (2016).